Microturbulence studies of pulsed poloidal current drive discharges in the reversed field pinch

D. Carmody, M. J. Pueschel, J. K. Anderson, and P. W. Terry

Articles you may be interested in

Density fluctuation measurements by far-forward collective scattering in the MST reversed-field pincha)
Rev. Sci. Instrum. **83**, 10E302 (2012); 10.1063/1.4728098

Investigation of turbulence in reversed field pinch plasma by using microwave imaging reflectometry
Phys. Plasmas **18**, 102315 (2011); 10.1063/1.3652848

Role of locked mode in the effectiveness of pulsed poloidal current drive regime in the reversed-field pinch
Phys. Plasmas **12**, 100703 (2005); 10.1063/1.2107027

Reduced intermittency in the magnetic turbulence of reversed field pinch plasmas
Phys. Plasmas **12**, 030701 (2005); 10.1063/1.1850475

Performance improvement conditions and their physical origin in the pulsed poloidal current drive regime of the reversed-field pinch device TPE-RX
Phys. Plasmas **11**, 5229 (2004); 10.1063/1.1796731

Microturbulence studies of pulsed poloidal current drive discharges in the reversed field pinch

D. Carmody,[a)] M. J. Pueschel, J. K. Anderson, and P. W. Terry
University of Wisconsin-Madison, Madison, Wisconsin 53706, USA

Experimental discharges with pulsed poloidal current drive (PPCD) in the Madison Symmetric Torus reversed field pinch are investigated using a semi-analytic equilibrium model in the gyrokinetic turbulence code GENE. PPCD cases, with plasma currents of 500 kA and 200 kA, exhibit a density-gradient-driven trapped electron mode (TEM) and an ion temperature gradient mode, respectively. Relative to expectations of tokamak core plasmas, the critical gradients for the onset of these instabilities are found to be greater by roughly a factor of the aspect ratio. A significant upshift in the nonlinear TEM transport threshold, previously found for tokamaks, is confirmed in nonlinear reversed field pinch simulations and is roughly three times the threshold for linear instability. The simulated heat fluxes can be brought in agreement with measured diffusivities by introducing a small, resonant magnetic perturbation, thus modeling the residual fluctuations from tearing modes. These fluctuations significantly enhance transport. © 2015 AIP Publishing LLC.
[http://dx.doi.org/10.1063/1.4905709]

I. INTRODUCTION

Gyroscale instabilities are widely believed to be responsible for anomalous transport in magnetic confinement devices. Such microinstabilities have been a focus of study in tokamaks for a long time but are a relatively new topic for the reversed field pinch (RFP). Historically, the RFP has been associated with large-scale tearing modes. It can now be operated at sufficiently reduced transport from global-scale modes to make (unaffected) contributions from gyroscale processes relatively more important. The technique for achieving these advances is pulsed poloidal current drive (PPCD), a current profile control technique that results in reduced global tearing mode activity and improved energy confinement time.[1] It is important to understand the role that microinstabilities play in this regime of operation. The full picture of microinstabilities in the RFP is still developing, and it is not yet clear which instabilities might be expected to dominate under various experimental conditions. Gyrokinetics, the primary tool used to evaluate the nature of microinstabilities, has shown that modes familiar from tokamaks—such as ion temperature gradient (ITG) modes, trapped electron modes (TEM), or microtearing (MT) modes—can also arise in the RFP, albeit with modified characteristics.[2–6] The RFP versions of these modes are generally marked by critical gradients that differ from the tokamak thresholds by a factor of the aspect ratio.

Previous microinstability work in the RFP has been done either in a generic, low-Θ equilibrium[2,6] (where $\Theta = \langle B_\theta \rangle^{\mathrm{wall}} / \langle B_\phi \rangle^{\mathrm{vol}}$ is the RFP pinch parameter and B_ϕ and B_θ are the toroidal and poloidal magnetic fields, respectively) or within the context of an internal transport barrier in a single-helical-axis (SHAx) regime.[3–5] In these regimes, ITG modes were seen to emerge as the dominant electrostatic instability, with MT arising at higher values of the normalized electron pressure β. As with critical gradients, β thresholds for

these instabilities occur at higher values relative to their tokamak counterparts, a feature associated with lower safety factor and stronger poloidal curvature.

In the present work we address for the first time the picture of microinstabilities and their associated turbulence in a set of PPCD discharges on the Madison Symmetric Torus (MST).[7] We find in this case that ITG and TEM are the dominant instabilities. Although ITG has been studied in some detail in the context of the RFP, less is known about the characteristics of TEM. TEM turbulence has been considered to be a source of electron heat transport in tokamaks, but its role in the RFP is not yet certain.

We also present nonlinear gyrokinetic simulations for one of these MST PPCD plasmas. Studies are conducted for a 500 kA PPCD plasma at the radial locations of $r/a = 0.86$ and $r/a = 0.91$, where a is the minor radius of MST and r is the minor radius of the flux surface. A significant upshift is seen in the threshold density gradient required for turbulence destabilization as compared to the linear critical value, a phenomenon akin to the Dimits shift in tokamak ITG turbulence.[8] The nonlinear upshift in TEM turbulence has been seen before in gyrokinetic simulations[9–11] in tokamaks and, like the Dimits shift, it is attributed to zonal flows. This is the first reported appearance of zonal flows in RFP simulations. In providing an additional region of parameter space, the RFP presents a new opportunity for exploring the physics of zonal flows and zonal density and their role in regulating transport. The zonal structures found here are strongly defined and able to largely counteract the large growth rates of the dominant linear instabilities. Strong zonal density structures are also observed, a feature that for certain regimes of TEM may become a means of nonlinear saturation.[12,13] Also explored is the effect of radial magnetic field perturbations and imperfect flux surfaces, which are found to diminish the strength of the zonal flow and lead to higher transport.

a)dcarmody@wisc.edu

The paper is structured as follows: First, in Sec. II, the details of the gyrokinetic model are briefly introduced, and the RFP equilibrium model implemented in the gyrokinetic code GENE[14,15]—which is used throughout this work—is described. In Sec. III, we present the results of linear gyrokinetic studies of two PPCD cases with plasma currents of 200 kA and 500 kA. This is followed in Sec. IV with the results of nonlinear simulations performed for the 500 kA case and a discussion of the relation between these results and experimental measurements from MST. Finally, all these results are summarized in Sec. V.

II. MODELING

In the gyrokinetic model, the fast gyromotion is averaged out. Because the phase space is reduced from 6D to 5D, gyrokinetics is the preferred method of exploring drift-wave dynamics for realistic experimental geometries and field configurations. In this work we present results from the gyrokinetic code GENE,[14,15] using a form of GENE's circular equilibrium model[16] that has been modified to accommodate RFP-specific physics. It is necessary to introduce these modifications due to the nature of the RFP magnetic equilibrium, in which the toroidal field B_ϕ is similar in magnitude to the poloidal field B_θ throughout much of the plasma volume. The modification employed here generalizes the equilibrium by including a polynomial factor $f(r/R_0)$ in the toroidal magnetic field that allows for variation with minor radius

$$\mathbf{B} = \frac{R_0 B_0}{R} |q| f(r/R_0) \left(\mathbf{e}_\phi + \mathbf{e}_\theta \frac{r}{R_0 \bar{q}} \right), \quad (1)$$

where r is the minor radius of the flux surface, a is the minor radius of the device, R_0 is the major radius of the device at the magnetic axis, B_0 is the on-axis background magnetic field, $R = R_0 + r \cos \theta$ is the distance of the flux surface under consideration from the center of the device, q is the safety factor at the center of the simulation domain, $\bar{q} = q\sqrt{1 - (r/R_0)^2}$, and $f(r/R_0)$ is taken to be a polynomial function (though other functions could easily be implemented as well). Also provided to GENE is the background magnetic shear, expressed as $\hat{s} = (r/q) dq/dr$. The difference between this and the original circular model is the inclusion of the factor $|q| f(r/R_0)$, which captures the dependence of the toroidal magnetic field on r and allows for a smoothly varying expression through the reversal surface, where q and the toroidal field go to zero. A choice of $f(r/R_0) = |q|^{-1}$ reproduces the original model. This adjusted circular model (ACM) has been benchmarked against the toroidal Bessel function model (TBFM).[6] As can be seen in Fig. 1, there is very good agreement for a low-Θ non-PPCD case where the latter is well-suited to describe the magnetic geometry. One advantage of the ACM is its ability to accommodate more general equilibria than the TBFM, such as high-Θ PPCD discharges where the TBFM breaks down. This allows the modeling of PPCD equilibria with parameters drawn directly from MST discharges. The limitations of the TBFM can be seen in Fig. 2, where we show a comparison of the fits provided by the ACM and the TBFM for an experimental PPCD
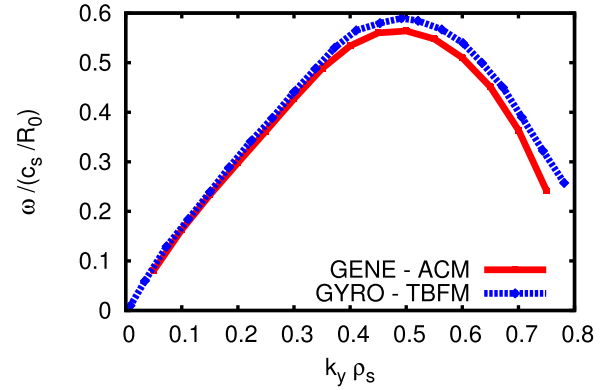

FIG. 1. Comparison of results from the TBFM implemented in Gyro (dotted blue line) and the ACM implemented in GENE (solid red line). Shown is the growth rate versus wavenumber. The important geometric parameters used in the two models are $q = 0.186$, $\hat{s} = -0.716$, $r/a = 0.5$, and $\Theta = 1.35$. The original Gyro results have been published in Ref. 2. An older version of the ACM (outlined in the text) is used in this figure.

magnetic equilibrium for MST. An earlier version of the ACM which has been employed to produce all numerical results reported in this paper differs from that described above in the use of q rather than $\bar{q}$ in Eq. (1). This results in a slight inaccuracy as $r/a \to 1$, but any difference in linear growth rates or nonlinear fluxes is less than 10% for the cases studied here.

The parameters for these simulations are drawn from experimental discharges on the Madison Symmetric Torus, an RFP with a major radius of 1.54 m and a minor radius of 52 cm. Two separate PPCD discharges are modeled here: a temperature-gradient-dominant 200 kA discharge and a density-gradient-dominant 500 kA discharge.[17] These discharges have been chosen because they represent different gradient regimes of PPCD. In performing a microinstability analysis of these discharges, we hope to assess the role of microturbulence in the transport characteristics of PPCD plasmas, as well as provide further information regarding observed
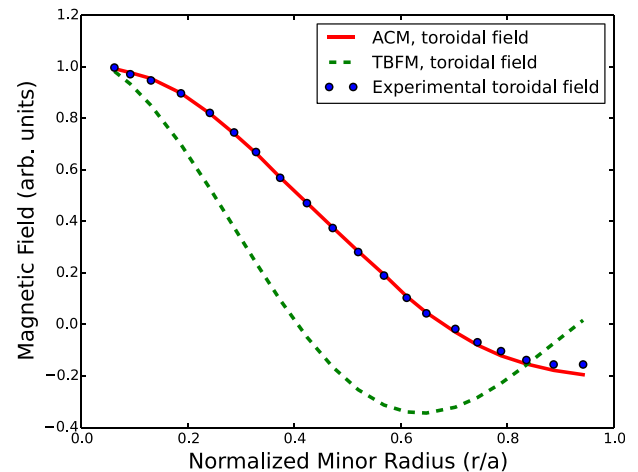

FIG. 2. The toroidal magnetic field for an experimental MST PPCD equilibrium (blue dots), the toroidal bessel function model (green dashed line), and the adjusted circular model (solid red line). The RFP pinch parameter Θ is 2.95 for this case. The TBFM is not an accurate model of the equilibrium for such large values of Θ, whereas the ACM reproduces the experimental data points very well.

TABLE I. Physical parameters for the two MST discharges studied in this work, as obtained from the MSTFit equilibrium reconstruction code.[18] It has been assumed that $T_i = 0.4T_e$, and therefore $R_0/L_T = R_0/L_{T_e} = R_0/L_{T_i}$. The polynomial fits $f(r/R_0)$ used for the two cases are $f(u \equiv r/R_0) = 1.4 - 3.7u + 92.2u^2 - 1074.7u^3 + 4726.9u^4 - 9139.6u^5 + 6542.3u^6$ for the 200 kA discharge and $f(u \equiv r/R_0) = 3.4 - 4.0u + 67.3u^2 - 956.6u^3 + 3517.6u^4 - 4338.4u^5 + 736.7u^6$ for the 500 kA.

Current	r/a	q	$\hat{s}$	β	ν_c	R_0/L_T	R_0/L_n
200 kA	0.61	0.04	−5.9	0.065	0.005	15.1	4.4
	0.79	−0.06	10.3	0.017	0.03	21.8	13.9
	0.84	−0.09	6.9	0.010	0.05	29.5	19.4
	0.89	−0.13	4.8	0.004	0.11	45.1	32.1
500 kA	0.76	−0.05	10.0	0.023	0.0012	11.3	19.7
	0.81	−0.09	6.7	0.015	0.0013	14.5	25.1
	0.86	−0.12	5.0	0.007	0.0014	25.4	34.8
	0.91	−0.16	3.8	0.002	0.0022	76.8	71.9

differences between the two cases. The set of parameters for each of these cases is presented in Table I. Listed are the plasma current for each of the two discharges, the normalized minor radius at which simulations were conducted, the safety factor q, the magnetic shear $\hat{s}$, the electron $\beta = 8\pi n_0 T_{e0}/B_{ref}^2$, the normalized temperature gradient $R_0/L_T = (R_0/T)dT/dr$ of both electrons and ions, and the normalized density gradient $R_0/L_n = (R_0/n_0)dn_0/dr$ at each of the radial locations. B_{ref} is the background magnetic field of the flux tube. The collisional frequency is given by $\nu_c = \pi \ln \Lambda e^4 n_0 R/\sqrt{8}T_{e0}^2$, where n_0 is the background density, e is the elementary electric charge, and $\ln\Lambda \approx 10$. Let us note that

the gradients at the outermost radial location of the 500 kA discharge are large enough to bring the ion gyroradius and the gradient length scale to within a factor of four of one another. Although this brings into question the validity of the local approximation, due to the large uncertainties in the experimental values of the transport fluxes, the local simulations are expected to yield sufficiently accurate results. More precise comparisons are an important area of future work as theoretical and diagnostic capabilities improve.

The 200 kA and 500 kA discharges have several key differences. At any given radial location, the 200 kA discharge has larger values of β and (normalized) temperature gradients that are stronger than the respective (normalized) density gradient. The 500 kA discharge, conversely, has density gradients that are larger than the temperature gradients. This difference is a determining factor in the type of instability that is dominant in each of these cases. It is important to note, however, that there is not an inherent relationship between plasma current and the dominant gradient. Thus, the dominant gradient is the defining characteristic of these discharges, and the current serves only as a convenient label.

The safety factor and electron temperature gradient profile for the 200 kA case are given in Fig. 3 and the safety factor and density gradient profiles for the 500 kA case are given in Fig. 4. Uncertainties are given for the temperature and density profiles. The estimated electron heat diffusivity for the 500 kA case is given in Fig. 5. The experimental profiles are generated using the MSTFit equilibrium reconstruction code,[18] which solves the Grad-Shafranov equation with input from external and edge diagnostics on MST. The
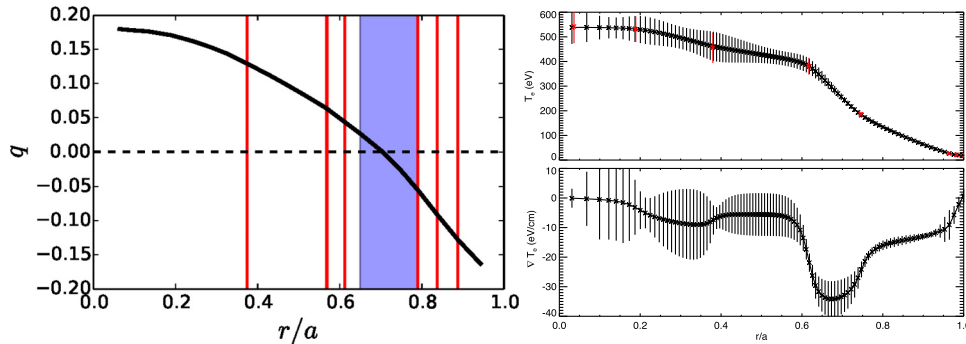

FIG. 3. Radial profiles for the safety factor (left), the electron temperature (top-right), and temperature gradient (bottom-right) for the 200 kA case. The red vertical lines on the safety factor profile indicate the radial locations at which simulations were performed. The blue shaded region indicates high shear ($|\hat{s}| \gtrsim 10$) and has been excluded from modeling. The red points on the temperature profile indicate experimental measurements from Thomson scattering.
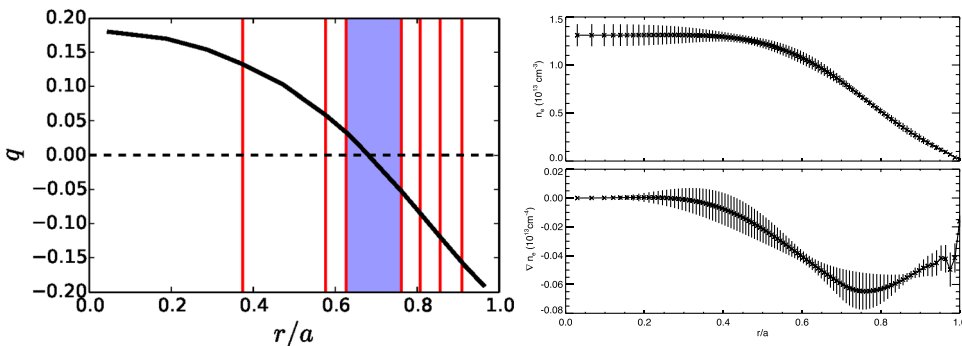

FIG. 4. Radial profiles for the safety factor (left), the density (top-right), and the density gradient (bottom-right) for the 500 kA case. The red vertical lines on the safety factor profile indicate the radial locations at which simulations were performed. The blue shaded region indicates high shear ($|\hat{s}| \gtrsim 10$) and has been excluded from modeling.
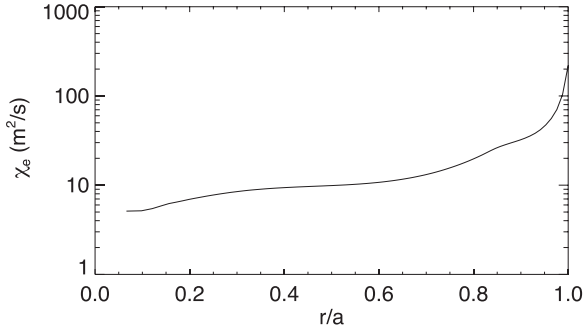
FIG. 5. Radial profiles of the electron heat diffusivity for the 500 kA case. This quantity is determined through the MSTFit equilibrium code and order of magnitude uncertainties exist on this value.

electron temperature profile is attained from Thomson scattering and soft-X-ray tomography. Density measurements are produced with far-infrared (FIR) interferometry/polarimetry. There are no ion temperature measurements for these discharges, but measurements from some improved confinement discharges have found core ion temperature to be on the order of 30%–50% of the core electron temperature.[1] Consequently, the ion temperature in the present work is assumed to be a constant factor of 0.4 times the electron temperature.

These experimental profiles are used in the GENE code as input for the collisionality, β, and gradient values, and as a magnetic field profile that is replicated using the analytic geometry model detailed above, with $f(r/R_0)$ as a sixth-order polynomial fitted to the reconstructed magnetic field. In all the work that follows, GENE is used in its radially local mode of operation, in which background quantities are assumed to vary linearly over the simulation domain. The nonlinear simulations described below have radial box sizes of ≈ 17–$20\rho_s \approx 17$–20 cm, and convergence with respect to the radial box size has been checked. Global simulations will become necessary once experimental measurements of heat and particle diffusivities are sufficiently precise to demand corresponding highly accurate theoretical predictions, but local simulations can still be expected to yield results here within experimental uncertainties, or within tens of percent of the global, physical fluxes.

An important distinction must be made here between the tokamak definition of magnetic shear $\hat{s}$ used above and the actual physical shear, referred to here as $\hat{s}_{\mathrm{RFP}}$. Magnetic shear, essentially a measure of the rate of variation of $k_\parallel \sim \mathbf{B} \cdot \nabla$ away from a rational surface, is a well-defined

quantity throughout the plasma volume. The quantity $\hat{s}$, however, relies on the tokamak expansion $B_\phi \gg B_\theta$ and has a singularity at the $q = 0$ surface. Near this surface, a new expansion of $k_\parallel$ can be made, with the approximation $B_\theta \gg B_\phi$, and an RFP-specific formula derived. The result of this is the expression $\hat{s}_{\mathrm{RFP}} = R dq/dr$, which holds as long as $|B| \sim B_\theta$ remains true. The relative ratio $\hat{s}/\hat{s}_{\mathrm{RFP}} = r/Rq$ provides a measure of the inadequacy of the tokamak shear definition near the reversal surface. Note that this inadequacy does not affect the accuracy of the GENE simulations: although $\hat{s}$ is provided as an input parameter to GENE's equilibrium model, it serves only as a means by which to define dq/dr ($dq/dr \equiv (q/r)\hat{s}$) as a diagnostic and for setting flux tube boundary conditions and does therefore not require inherent tokamak assumptions. However, challenges may nevertheless arise in numerical computation. At the reversal surface, for instance, where $q \to 0$ and $\hat{s} \to \infty$, even though dq/dr is well-defined, the quantity $(q/r)\hat{s}$ is not. High values of $|\hat{s}|$, through the parallel boundary condition that couples k_x modes, require high x resolution, placing a practical constraint on the ability of GENE to model cases with very large $|\hat{s}|$. A region of very high $|\hat{s}|$ (where $|\hat{s}| > 10$) around the reversal surface has therefore been excluded from these modeling studies as a matter of practicality. This region is an area of some interest in the RFP, and modeling it remains an important avenue for future work.

III. LINEAR RESULTS

The dominant instabilities for the 200 kA and 500 kA cases are, respectively, ITG and TEM. A plot of growth rates versus minor radius is given in Fig. 6 for both the 200 kA and 500 kA discharges. All modes show typical ballooning parity in the eigenmode structure, marked by even parity in electrostatic potential Φ and odd parity in magnetic potential $A_\parallel$. Both discharges show that growth rates are higher at larger radii, which correspond to larger values of the normalized gradients.

For the 200 kA discharge, it is found that the dominant modes for $r/a \leq 0.84$ have frequencies in the ion direction and can be categorized as ITG. The mode at $r/a = 0.89$ for the 200 kA case displays characteristics of an ITG/TEM hybrid, including complicated gradient dependencies and smooth transitions in the frequency from ion to electron direction with the variation of parameters. This shall be further elaborated on below.
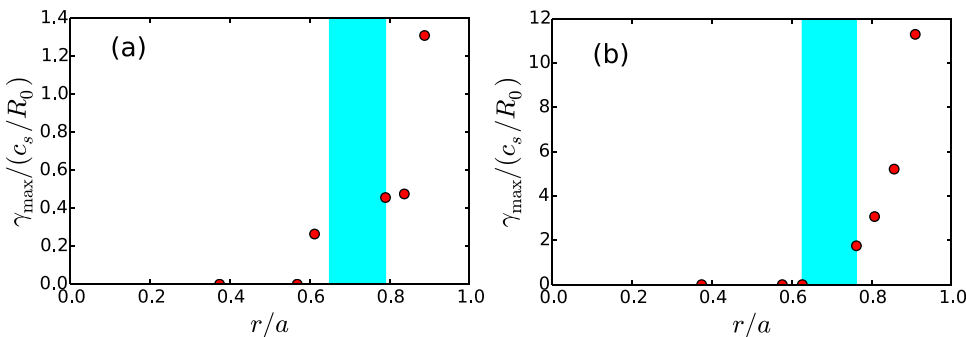

FIG. 6. Peak growth rates versus minor radius for the 200 kA (a) and 500 kA (b) cases. The blue shaded region indicates high shear ($|\hat{s}| > 10$) and has been excluded from modeling. γ_{max} is the maximum growth rate attained from a k_y scan.
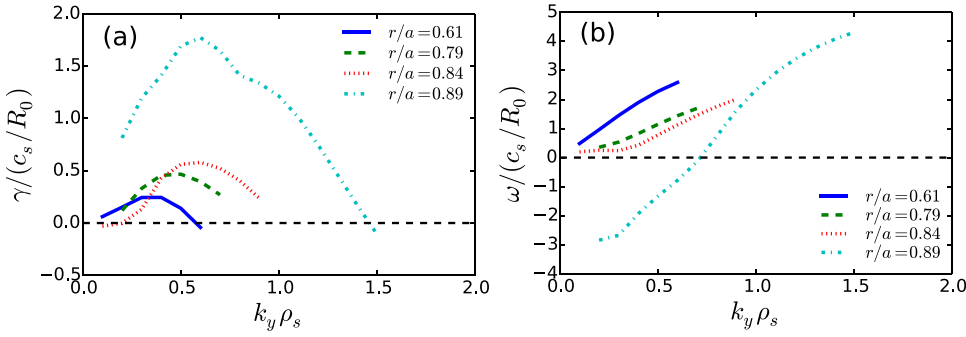
FIG. 7. Growth rates (a) and frequencies (b) as functions of wavenumber at different radial locations for the 200 kA case. For $r/a \leq 0.84$, the modes are in the ion direction and interpreted to be ITG. The outermost radius displays a smooth transition from electron to ion direction with wavenumber and is identified as an ITG/TEM hybrid.

The growth rates and frequencies as functions of the wavenumber $k_y \rho_s$ (where k_y is the binormal wavenumber, $\rho_s = (T_{e0}/m_i)^{1/2} m_i/eB_{\text{ref}}$ is the ion sound gyroradius, and m_i is the ion mass) are presented for the 200 kA case in Fig. 7 for different radial locations. In our convention, a positive frequency indicates the ion diamagnetic direction. There is an increase in growth rates and a general widening of the spectra to high k_y as we move outward in radius, as well as a shift in the peak of the spectrum. For $r/a \leq 0.84$, the instability is identified as the ion temperature gradient mode on the basis of its frequency in the ion direction and an instability threshold in ion temperature gradient scale length (see Fig. 8). The results of density gradient scans are presented in Fig. 9. The gradient scans are performed at the k_y value of the peak growth rate, which occurs in the range of $k_y \rho_s = 0.4$–0.6 for the ITG modes and $k_y \rho_s = 0.6$ for the hybrid ITG/TEM. As can be seen in Fig. 8, the critical gradient values for the ITG fall within the range $R_0/L_{Ti} \approx 10$–25, while the outermost radius shows no critical value. The instability that is present at $r/a = 0.89$ is identified as a hybrid ITG/TEM.

It has been seen in kinetic microinstability calculations that $\eta_i \equiv (d\ln T_{i0}/dr)/(d\ln n_0/dr)$ is an important parameter in determining the dominant instability. The dominant

instability tends to be ITG for η_i above a critical value of $\eta_{ic} \sim 1.2$–1.4 and TEM for $\eta_i < \eta_{ic}$.[19] The η values ($\eta \equiv \eta_e = \eta_i$) as a function of radial location for the two discharges considered in this work are given in Fig. 10, where it can be seen that the 200 kA case lies above the region $\eta_{ic} \sim 1.2$–1.4 and the 500 kA case lies predominantly below. Importantly, there are some parameter regimes in which these two modes can merge and form a hybrid. The hybrid tends to be characterized by smooth transitions in the frequency from negative to positive with the variation of the gradient parameters, while marking an exceptional point in parameter space.[21] Additionally, the analogously defined quantity $\eta_e \approx 1$ represents an important transition between density-gradient-driven TEM and temperature-gradient-driven TEM,[20] a differentiation that has important consequences for the physics of nonlinear saturation, as will be discussed in more depth in Sec. IV.

Moving on to the characteristics of the other MST discharge, the wavenumber spectrum is given for the 500 kA case in Fig. 11. The spectrum can be seen to peak around $k_y \rho_s \approx 0.6$ for each of the radial locations. Although the real frequencies for these modes are predominantly in the electron direction, at the outermost radial locations, $r/a = 0.86$
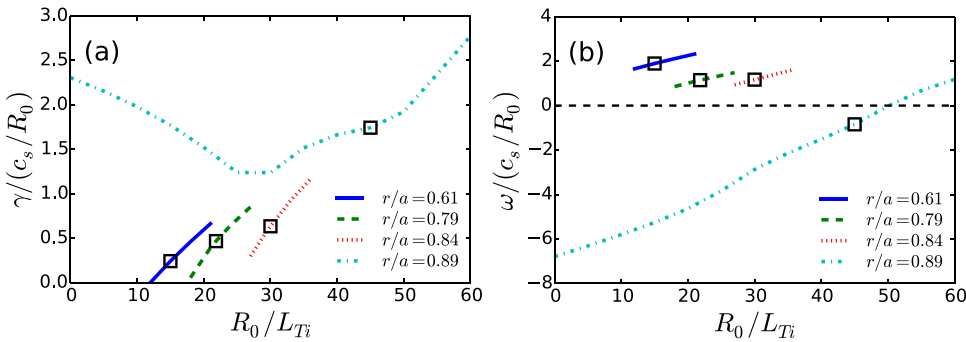

FIG. 8. Growth rates (a) and frequencies (b) plotted against ion temperature gradient for the 200 kA case for multiple radial locations. The modes at $r/a \leq 0.84$ display a strong dependence on this gradient and are identified as ITG. The black squares denote growth rates and frequencies at the experimental gradients.
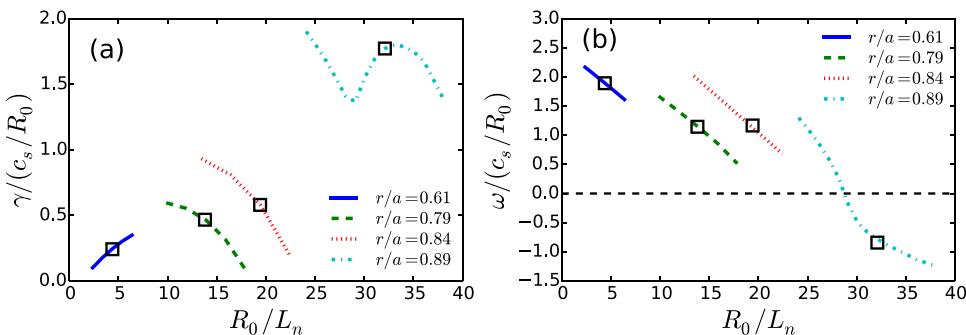

FIG. 9. Growth rates (a) and frequencies (b) plotted against density gradient for the 200 kA case. The complicated dependence of the instability at $r/a = 0.89$ and a real frequency that transitions smoothly from ion direction to electron direction are characteristics for a hybrid mode. The black squares denote growth rates and frequencies at the experimental gradients.
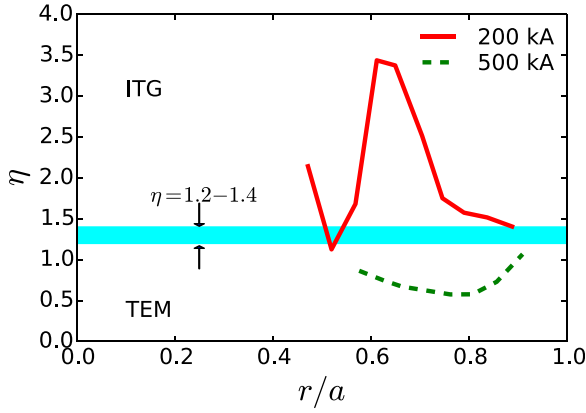
FIG. 10. The value of $\eta \equiv (d\ln T/dr)/(d\ln n_0/dr)$ versus minor radius. $T_i \propto T_e$ in these runs, so $\eta = \eta_e = \eta_i$. The shaded region indicates the critical range $\eta_i = 1.2–1.4$, above which instabilities tend to be ITG and below TEM, in relatively good agreement with the observations from the present simulation data. Near the threshold, the dominant instabilities may become hybrid modes with characteristics of both ITG and TEM.

FIG. 13. Growth rates plotted against β for the 200 kA case. All modes show little variation with β, a characteristic that is related to a high β threshold for electromagnetic instabilities. The frequencies are similarly unaffected by variations of β.

and $r/a = 0.91$, the frequency becomes positive at high k_y. This mode is often referred to as the "ubiquitous mode" and is a feature of collisionless TEM in the high k_y limit. This behavior has been described previously in numerical calculations and gyrokinetic simulations[9,19,20] and analyzed in depth in Coppi *et al.*[26]

A density gradient scan is performed at the wavenumber of the peak growth rate for each of the radial locations from Fig. 11. The results are presented in Fig. 12, where it can be seen that there is a strong dependence of the growth rate on density gradient with a critical gradient occurring around $R_0/L_n \sim 15$ for each radial location. For this reason, and a real frequency in the electron direction, these modes are identified as density-gradient-driven TEM. These modes show some dependence on ion and electron temperature gradients,
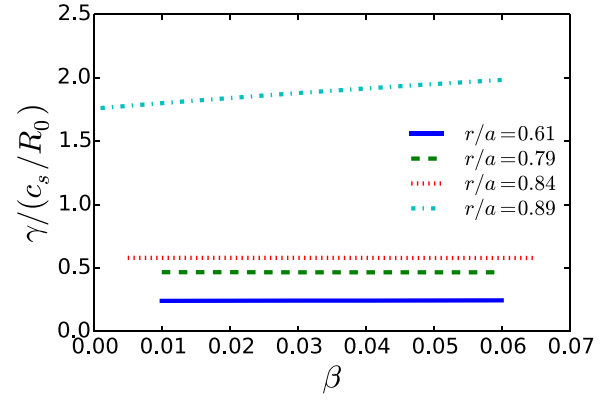
but no critical values. It should be noted that for this discharge, the values of collisionality obey the relationships $\nu^* \equiv \nu_c/\omega_b \ll 1$ and $\nu_c/\omega \ll 1$, with ω the real frequency of the instability and the bounce frequency $\omega_b \equiv \epsilon^{1/2}v_{te}/qR_0$ defined in terms of the aspect ratio $\epsilon = r/R_0$ and the electron thermal velocity $v_{te} = (T_{e0}/m_e)^{1/2}$. This is well in the collisionless regime. For the radial location $r/a = 0.86$, there is an ion mode that is dominant at low values of the density gradient and is likely ITG.

A. β dependence

These modes all demonstrate an independence with respect to plasma β, a behavior that can be seen for the 200 kA case in Fig. 13. Although weak β dependence is a characteristic expected of TEM, ITG is known to be stabilized by increasing β, both linearly[2,22,23] and nonlinearly.[24,25] An
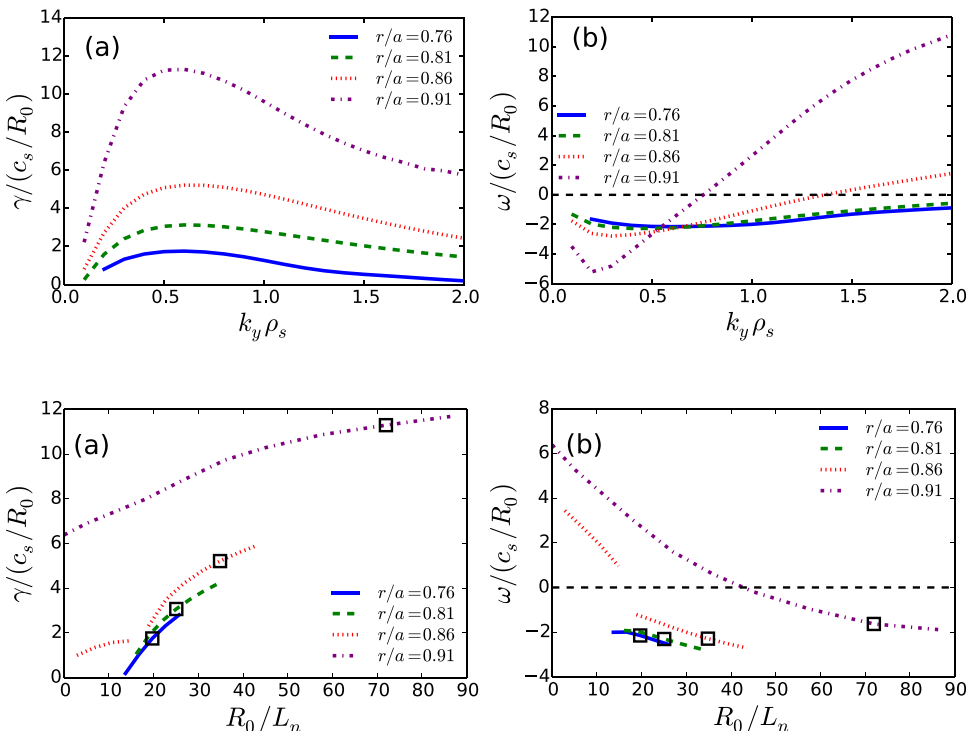

FIG. 11. Growth rates (a) and frequencies (b) as functions of wavenumber at different radial locations for the 500 kA case. These modes are driven by the density gradient and are identified as TEM; only at the outer radii and higher k_y can signatures of ubiquitous modes be seen.

FIG. 12. Growth rates (a) and frequencies (b) plotted against density gradient for the 500 kA case. The dominant modes for the nominal parameters show a strong dependence on density gradient and are identified as density-gradient-driven TEM. The black squares denote growth rates and frequencies at the experimental gradients.

important conclusion to draw from these results is that, despite operating at a β that is considered high in the context of tokamaks, the instabilities present in PPCD plasmas are predominantly electrostatic. Notably absent is KBMs and MT modes. All RFP modeling work has thus far shown no evidence of KBMs, a mode known to arise in finite-β simulations in the tokamak at a typical β of 0.6%–2%.[23,27,28] The absence of KBMs in the RFP may be explained as a consequence of two geometric properties: high magnetic shear and low safety factor. In the tokamak, KBMs are seen to emerge at some considerable fraction (generally about 70%–100%) of the ideal ballooning mode critical β.[23,24,29] In the RFP, however, the critical β for the ideal ballooning mode increases in regions of high shear.[30] If KBMs are tied to this threshold in a similar way, then it can be expected that the KBM threshold will increase as well. Using the plasma ballooning parameter $\alpha_{MHD} = \beta q^2 (R_0/L_n + R_0/L_{Te} + (R_0/L_n + R_0/L_{Ti})T_i/T_e)$ and a naive use of the tokamak threshold for the critical MHD ballooning limit $\alpha_{MHD}^{crit} = 0.6\hat{s}$,[31] we may make an estimate of the critical MHD ballooning β. This yields a value of $\beta_{crit}^{MHD} \approx 750\%$ for the 200 kA $r/a = 0.84$ case and generally above 50% for all cases studied here. The use of $\hat{s}_{RFP}$ in place of $\hat{s}$ in the α-threshold expression reduces these limits, generally by a factor of 2–3. Even so, these estimates suggest that the experiment operates well below the range of β where effects tied to the KBM threshold are likely to play a significant role. In a related matter, the same geometric effects that cause the KBM threshold to be pushed up are likely also responsible for a higher threshold for shear Alfvén waves, and therefore a lack of ITG stabilization with β.[2] This explains why, in the parameter regime of these discharges, the instabilities remain electrostatic for experimentally relevant β.

Previous work in the RFP has also shown signs of MT,[2,3] which is not present in these PPCD simulations. This may also be explained by the effect of high magnetic shear. It has been demonstrated that, in the RFP, MT is stabilized by high values of magnetic shear[3] and by high values of the RFP pinch parameter Θ, which also corresponds to high values of shear.[2] In the present PPCD discharges the areas most likely to be unstable to MT (regions of high β and high electron temperature gradient) are also regions of high magnetic shear. Under these circumstances, the stabilizing effects of the shear are strong enough to overcome the MT instability drive.

IV. NONLINEAR RESULTS

We report results from the first nonlinear gyrokinetic simulations in PPCD plasmas. These results come from the 500 kA case at $r/a = 0.86$ and $r/a = 0.91$. The relevant physical parameters for these runs can be found in Table I.

First, we will make some comments on the resolution requirements. Nonlinear gyrokinetics in the RFP is very resource-intensive, requiring radial resolutions in excess of similar tokamak cases. This is largely due to the high magnetic shear of the RFP, which, because of the parallel boundary condition (requiring for some quantity F, $F(k_x, k_y, z + L_z) = F(k_x', k_y, z) \exp[2\pi i k_y \hat{s} r_0]$, with $k_x' = k_x + 2\pi\hat{s}k_y$ and L_z the

parallel box size[34]), sets restrictions on the radial box size and grid spacing. High radial resolution, in turn, results in increased computational expense and more processor-hours required for saturation. For the $r/a = 0.86$ case, the following set of resolutions was used: 24 k_y modes, 24 parallel grid points, 32 parallel velocity grid points, 12 magnetic moment grid points, and 284 radial grid points. A time trace of the saturated transport levels for a sample run is given in Fig. 14. Completing a nonlinear run such as this takes roughly 100 000 processor hours on a Cray XT5 computer. The $r/a = 0.91$ case, where $|\hat{s}|$ is smaller, requires less radial resolution and can be performed with fewer hours.

As discussed in Sec. III, the dominant linear instability for these sets of parameters is a density-gradient-driven TEM. The nonlinear evolution shows a phase of strong linear growth, at which point nonlinear processes arise and act to saturate the turbulence and suppress transport fluxes—note that the so-called overshoot is larger than in typical tokamak simulations. This nonlinear saturation is due to the emergence of zonal flows, $k_y = k_\parallel = 0$ fluctuations that provide an energy damping mechanism[38] and place limits on radial transport.[32,33] Zonal flows are known to be an important element of nonlinear saturation and the formation of transport barriers.[35]

The transport spectra are given in Fig. 15 for both cases. In comparison, electrostatic particle transport and electrostatic electron heat transport (other transport channels being negligible) peak at around $k_y \rho_s = 0.2$, with minimal transport at the highest k_y. This is significantly below the peak of the linear growth rate spectrum at $k_y \rho_s = 0.6$.

A nonlinear gradient scan was performed for the $r/a = 0.86$ case, the results of which can be seen in Fig. 16. This figure shows a scan of the density gradient, along with the respective linear growth rates for comparison. Electron heat transport outweighs ion heat transport, and despite operating at β values (given in Table I) that would be considered large in the context of the tokamak (as was discussed in Sec. III A), the transport is almost entirely electrostatic. Furthermore, there is a strong shift in the critical gradient as compared with
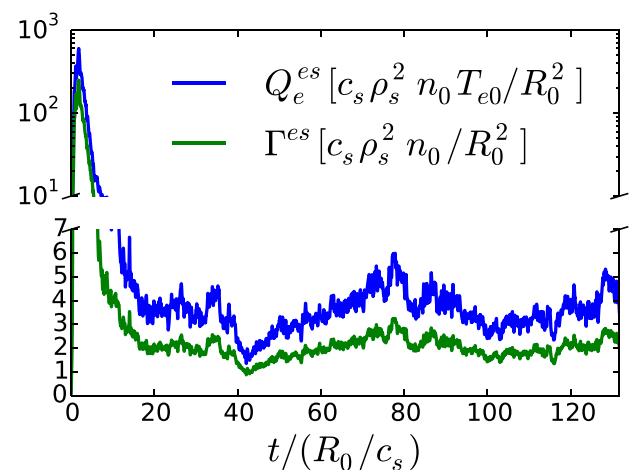

FIG. 14. A time trace of the nonlinear fluxes for a density gradient of $R_0/L_n = 58.8$. The dominant channels are electron heat flux Q_e^{es} (blue) and particle flux Γ^{es} (green). A vertical break is included to show the strength of the overshoot as compared to the variability of the saturated state.
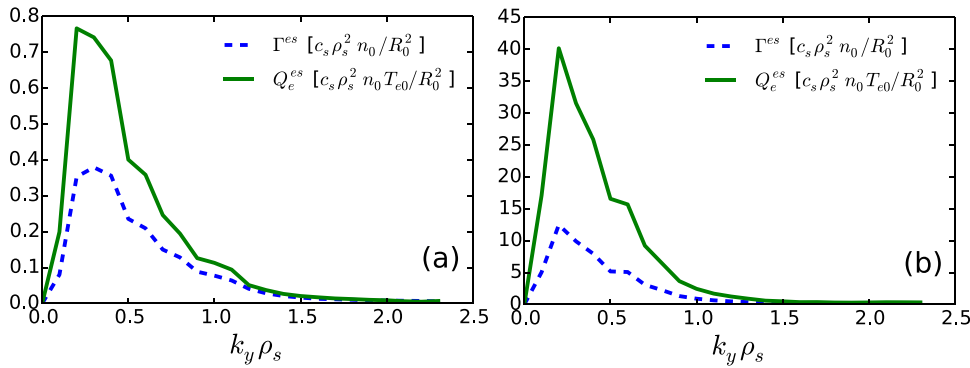
FIG. 15. The flux spectra for (a) $r/a = 0.86$ and $R_0/L_n = 52.3$ and (b) $r/a = 0.91$ and $R_0/L_n = 71.9$. Shown are the electrostatic particle flux Γ^{es} (blue dashed line) and the electrostatic electron heat flux Q_e^{es} (green solid line). At $r/a = 0.86$, the spectra peak at $k_y\rho_s = 0.3$, while at $r/a = 0.91$ the peak shifts to $k_y\rho_s = 0.2$. In comparison, the linear growth rates peak at $k_y\rho_s = 0.6$ for both cases.

the linear case, with the nonlinear threshold occurring around $R_0/L_n = 35$ as compared to the linear threshold of $R_0/L_n \approx 10$–15. This nonlinear upshift in the critical gradient has been discussed before in the context of TEM turbulence in the tokamak,[9] but has yet to be addressed in the RFP where a different magnetic geometry may lead to different characteristics. The magnitude of the shift seen in Fig. 16, where the nonlinear threshold is roughly 3 times the linear one, an upshift comparable to that found in Alcator C-Mod.[10,11] It has been shown that, in the tokamak, the TEM upshift decreases with increasing safety factor.[11] This would be consistent with a larger upshift observed in the RFP accompanying its smaller safety factor, although there may be other important factors as well. This suggests that zonal flows may have a similar, or perhaps stronger, impact in the RFP as compared to the tokamak.

As with the tokamak case, the shift here is attributed to the presence of strong zonal flows, which are known to moderate linear instabilities and reduce transport levels. Numerical studies of a variety of both gyrokinetic and fluid models have found zonal flows to play a key role in the transfer of energy to damped modes, an important process for nonlinear saturation.[36–40] Clear evidence for zonal flows can be seen in the contours of the electrostatic potential Φ,
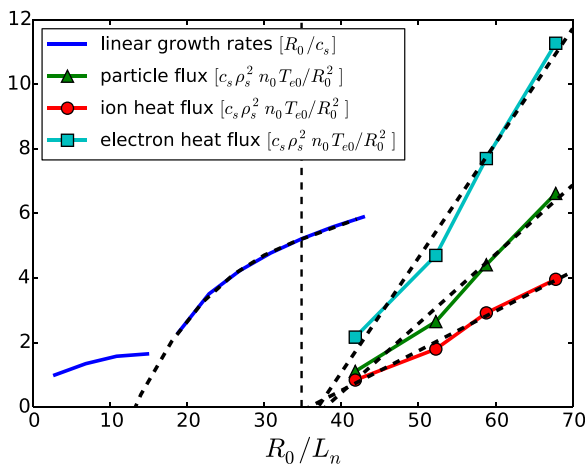

FIG. 16. Electron heat and particle fluxes are plotted as a function of density gradient for the 500 kA case at $r/a = 0.86$. The linear growth rates for these parameters are also shown for comparison. Straight line fits have been applied to the fluxes, and a cubic fit has been applied to the TEM portion of the linear growth rate curve. The onset for the nonlinear fluxes occurs at $R_0/L_n \approx 37$, roughly a factor of 3 greater than the linear threshold of $R_0/L_n \approx 13$. The vertical dashed line indicates the nominal experimental value of R_0/L_n.
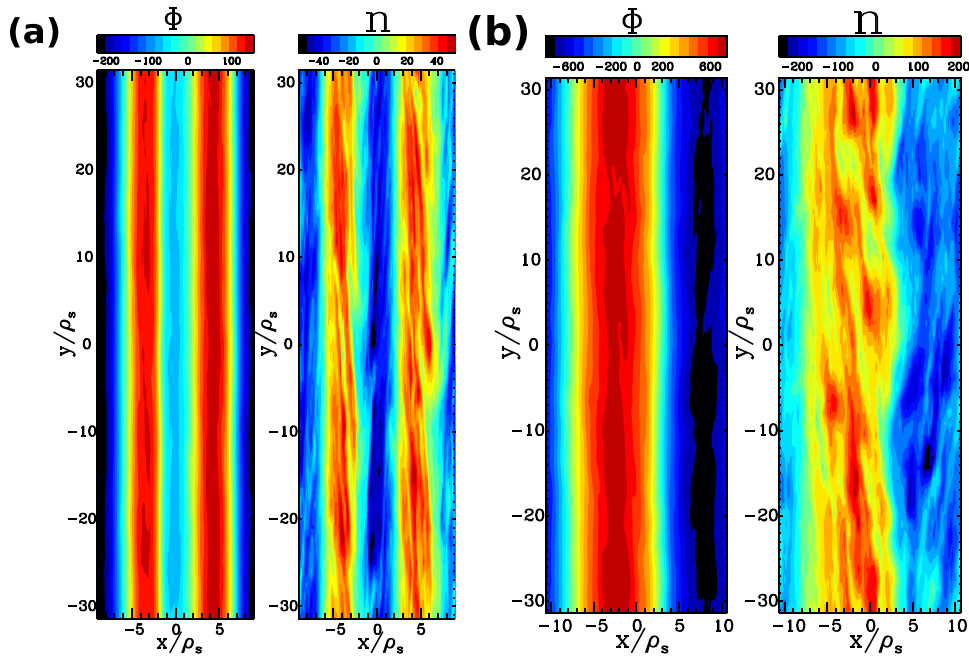
which is given in Fig. 17 along with the contours for the perturbed electron density n_e: A strong contribution from the $k_y = 0$ mode is apparent in the Φ contours. Similarly, $k_y = 0$ features in the density contours indicate a zonal density structure. The normalized density amplitudes are weaker than the Φ amplitudes by roughly a factor of four, indicating the dominance of zonal flows over zonal density, although in some regimes (though not any of those observed in the context of the present study), particularly those where temperature gradients are much stronger than density gradients, the role played by zonal flows in saturation is known to be much diminished, and zonal density emerges as the expected dominant saturation mechanism.[13]

An important measure of the zonal flow activity is the $\mathbf{E} \times \mathbf{B}$ shearing rate $\omega_E = d^2\Phi_{zon}/dx^2$, where Φ_{zon} is the zonal component of the electrostatic potential. The shearing rate is a well known causative effect for transport reduction. However, it is also a proxy for the efficiency of zonal-flow-catalyzed energy transfer to damped modes. Zonal flows are generally considered to be important for nonlinear saturation when the shearing rate is at least as large as the maximum linear growth rate when taking into account finite frequency corrections.[32,41,42] Though these corrections are not included in this analysis, ω_E is consistently an order of magnitude larger than the peak linear growth rate, a commonly used criterion to determine zonal flow impact without utilizing the aforementioned finite-frequency corrections.[20,23] Fig. 18(a) shows nonlinear density gradient scans at several different values of $\hat{s}$, with the fluxes increasing as $\hat{s}$ is reduced. In Fig. 18(b), we plot the ratio ω_E/γ_{lin} of the zonal flow shearing rate and the peak linear growth rate for these same cases. As shear is reduced, this factor decreases, a result of both an increase in linear growth rate and a decrease in ω_E. At $\hat{s} = 2.5$, the shearing rate falls below $10\gamma_{lin}$, a transition that is associated with higher fluxes (as can be seen in Fig. 18).

A nonlinear upshift in the critical density gradient for TEM turbulence has been seen before in gyrokinetic simulations in the context of the tokamak[9] and is seen as a similar process to the Dimits shift observed in the case of ITG turbulence.[8] As in the Dimits shift, zonal flows play an important role in the suppression of transport fluxes, and it has been found that both magnetic shear and the electron temperature gradient can affect the characteristics of zonal flows in TEM turbulence.[12] In particular, the role of zonal flows in saturating TEM turbulence has been found to depend on η_e, with zonal flows important for $\eta_e < 1$ and relatively unimportant

FIG. 17. Contours of electrostatic potential Φ and electron density n for the 500 kA case at (a) $r/a = 0.86$ and $R_0/L_n = 52.3$ and (b) $r/a = 0.91$ and $R_0/L_n = 71.9$. Strong vertical features ($k_y = 0$) in Φ are indicative of zonal flow activity, while the density contours show some (but relatively weaker) zonal structures as well.
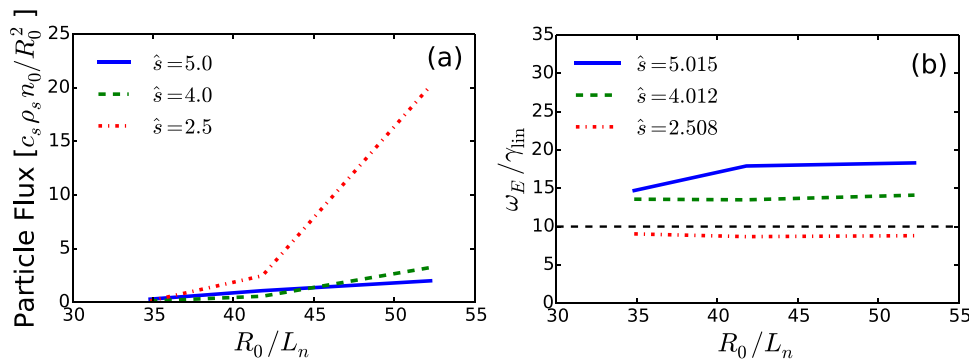

FIG. 18. (a) Particle flux versus density gradient for three different values of magnetic shear, $\hat{s} = (r/q)(dq/dr)$. (b) Zonal flow shearing rate divided by linear growth rate versus density gradients for different values of magnetic shear. For $\hat{s} = 2.5$, the zonal flow shearing rate drops below $10\gamma_{\rm lin}$ (indicated by the black dashed line in the lower plot) and the flux substantially increases. Other parameters are as given for the 500 kA case at $r/a = 0.86$.

above this critical value, where the TEM is driven by the electron temperature gradient rather than the density gradient.[20] It has been suggested that zonal density generation is responsible for nonlinear saturation in the absence of zonal flows.[13] The η_e radial profile for the 500 kA is given in Fig. 10. The value of η_e only becomes greater than 1 above $r/a \simeq 0.9$, suggesting that zonal density may play a greater role towards the edge in MST. Indeed, as can be seen in Fig. 17, the relative strength of the zonal density structure as compared to zonal flow is larger at $r/a = 0.91$ (factor of $\approx 1/3$) than at $r/a = 0.86$ (factor of $\approx 1/4$). It should be noted that the strength of the peak density fluctuations in Fig. 17(b) may be large enough to violate the δf ordering inherent in GENE, but this is an extreme case, and it serves only to restrict quantitative comparisons to within a factor of two.

Another important result of these simulations is that the nonlinear threshold occurs at roughly the nominal experimental value, indicated by the vertical dashed line in Fig. 16. A similar result was found in tokamaks providing evidence of the nonlinear upshift.[11] This suggests that the experiment may be operating near a critical threshold and microinstability-driven turbulence may be playing an important role driving transport. Although the experiment appears to be operating near marginal stability, the transport seen in the simulations

falls significantly below that observed in experiments on MST. At a gradient of $R_0/L_n = 52.3$, which is 50% larger than the nominal experimental density gradient, the value of the electron electrostatic heat diffusivity is found to be $\chi_e^{es} = 0.3 \, \text{m}^2\text{s}^{-1}$, much lower than the experimental value of $\sim 30 \, \text{m}^2\text{s}^{-1}$ (seen in Fig. 5), although there are large uncertainties in the experimental estimate. Further out, at $r/a = 0.91$ the electron heat diffusivity at experimental gradients is $\chi_e^{es} = 2.9 \, \text{m}^2\text{s}^{-1}$, still well below experimental estimates. As demonstrated below, this gap can be bridged by taking into account residual magnetic fluctuations from tearing mode activity and their deleterious impact on zonal flows.

A. Magnetic perturbations and transport

Thus far, we have not accounted for the role played by magnetic stochasticity, an important contributor to transport processes in the RFP, even in the relatively well-behaved PPCD discharges. The effect of stochastic fields in gyrokinetic simulations has been a topic of recent interest,[44–47] revealing that self-consistent magnetic stochasticity may be ubiquitous in tokamak gyrokinetic simulations, arising at low values of β due to the nonlinear excitation of linearly damped microtearing modes. In the present work,
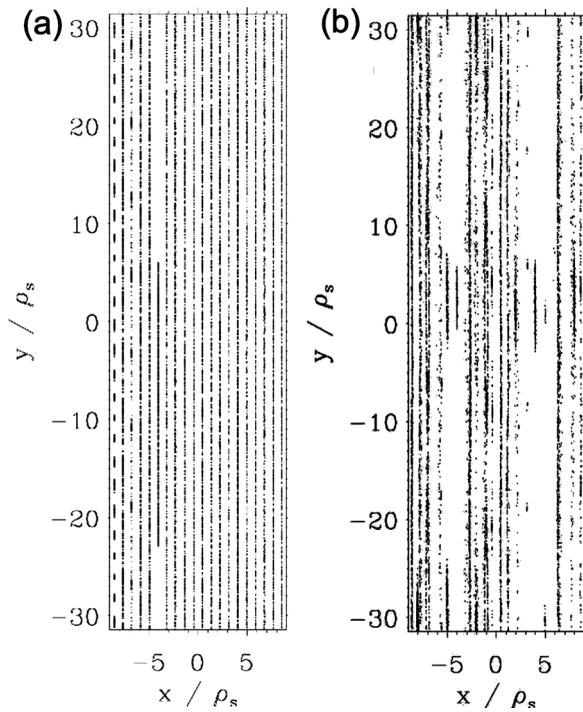
FIG. 19. Poincaré puncture plots without (a) and with (b) a small added resonant perturbation to $A_\parallel$. Though the flux surfaces are still largely intact, the imposition of a small resonant radial magnetic field leads to the reduction of zonal flows and a large increase in transport. More details on the field line integration routine may be found in Ref. 57.

at $\beta = 0.7\%$, there is virtually no stochasticity inherent in the nonlinear simulations (see Fig. 19(a)), an outcome related to the increased MHD β limit discussed above. Clearly, the flux surfaces are almost completely intact, and the radial motion of particles streaming along perturbed field lines is essentially negligible. As a consequence, a variety of models treating the physics of magnetic perturbations are not applicable here, at least as long as only self-consistent perturbations are considered (see below). Such models require a fully stochastic nonlinear state of the perturbed flux surfaces—compare the (quasi-)linear and nonlinear electron flutter transport reported in Ref. 23. The degree to which these simulations are in a magnetically nonlinear state can be assessed through the evaluation of the contribution to the overall electromagnetic heat conductivity from the Rechester-Rosenbluth term[56] $\chi_e^{em} = \chi_{e\parallel}$ $\langle (\tilde{B}_x / B_{\text{ref}}) \rangle$, where $\chi_{e\parallel} \approx k_\parallel^{-1} (T_e/m_e)^{1/2}$. The transport predicted by this formula is far larger than that observed in the simulations, therefore it is reasonable to conclude that this term is not contributing to transport and quasilinear approximations may be used. Similarly, the predictions in Refs. 51 and 52 for B_x and related quantities do not hold here. However, the effect of residual tearing mode fluctuations is neglected. In standard discharges of the RFP, large-scale tearing modes, driven by the gradient in the current profile, produce stochastic magnetic fields.[53,54] Though this is largely controlled with PPCD, some stochasticity still remains,[43,55] and even at the radii considered here (where no fully stochastic field is measured), significant radial excursion of perturbed field lines occurs.

To address the issue of how this may affect microturbulent transport, we have imposed an artificial Gaussian perturbation on $A_\parallel$ in the z direction with $k_x = 0$ and $k_y = 0.2$, corresponding to a resonant B_x perturbation. The strength of this perturbation can be tuned to introduce a small radial displacement of the magnetic field, in this case leading to a magnetic diffusivity[44,56] of $D_m \sim 10^{-8}$ m. Fig. 19(b) shows the Poincaré plot associated with such a perturbation. The level of diffusivity introduced here is not enough to lead to true stochastization, but instead serves only to slightly degrade the flux surfaces.

There are several outcomes of introducing this resonant perturbation. One is the generation of a small amount of electromagnetic heat flux ($\chi_e^{em} = 3.2 \, \text{m}^2 \text{s}^{-1}$, as compared to $\chi_e^{em} \approx 0$ without the imposed perturbation.) Another, more important effect is an increase in the electrostatic heat flux, which increases by more than a factor of ten to $\chi_e^{es} = 25.2 \, \text{m}^2 \text{s}^{-1}$. This result can be seen in Fig. 20, which shows a time trace comparing the particle and heat fluxes before and after the addition of the perturbation. This increase in transport is due to the weakening of the zonal flows responsible for saturation, an effect known from studies of the nonzonal transition in tokamaks.[48–50,52] Fig. 21 shows contours of Φ and n for the case with imposed diffusivity, and it can be seen that the $k_y = 0$ structures are very much diminished, both in their absolute amplitudes—despite the increased χ_e—and in relation to the structure with $k_y \neq 0$. The degradation of the zonal flow is caused by the magnetic flutter induced loss of electrons from their radial surface, which creates a radial current that diminishes the zonal potential.[48] The large effect of radial magnetic field perturbations in the present work is likely due to both the strength of the zonal flows as well as the effectiveness of stochasticity in their damping. In particular, the zonal flow decay time as reported in Refs. 48 and 49 is linear in q, suggesting that for a large radial region in MST (where q is much lower than in a tokamak), this process is very effective. This analysis suggests that the experimental fluxes may be accounted for by drift wave turbulence in the presence of a small amount of
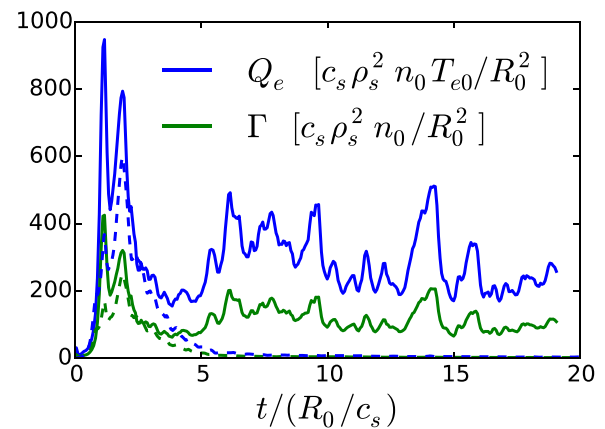

FIG. 20. Electron heat (blue) and particle flux (green) before and after the inclusion of an imposed perturbation on $A_\parallel$. The imposed magnetic diffusivity weakens zonal structures and results in a large increase in the transport levels. Shown are the fluxes after instituting the artificial perturbation (solid lines) as compared with those same quantities before (dashed lines).
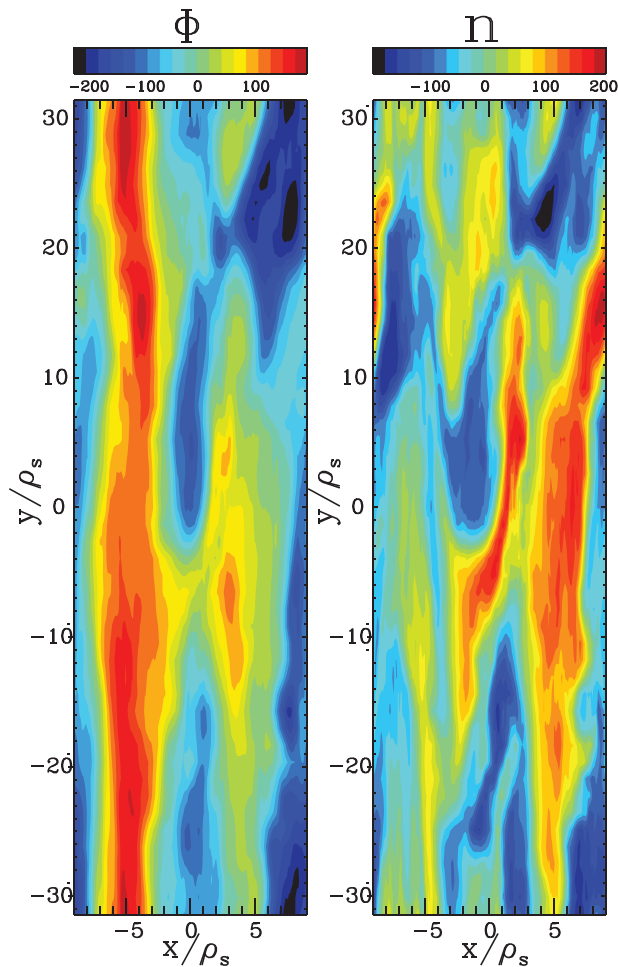
FIG. 21. Contours of Φ and n for the $r/a = 0.86$ case where a resonant $A_\parallel$ perturbation has been implemented to introduce a small radial perturbation to the magnetic field. The effect is to greatly diminish the zonal structures evident in Fig. 14(a).

magnetic diffusivity. However, the value of D_m chosen above serves only as a rough estimate, as the experimental quantity is largely unknown for these discharges.[55] Since there is such sensitivity of these results to the level of magnetic diffusivity, it is highly important to determine this value experimentally as precisely as possible. This presents an area of interest for future work in both experiment and numerical simulation.

V. SUMMARY

We have performed a series of linear and nonlinear gyrokinetic simulations in PPCD discharges of MST plasmas and characterized the gyroscale processes. A temperature-gradient-dominant discharge (with plasma current 200 kA) has been found to be linearly unstable to ITG and a hybrid ITG/TEM, while the density-gradient-dominant discharge (with plasma current 500 kA) has been found to be unstable to a density-gradient-driven TEM. Consistent with tokamak-based expectations, the parameter η_i is found to be an important determining factor in the dominant instability type, with TEM prevalent for $\eta_i \lesssim 1.3$ and ITG prevalent for $\eta_i \gtrsim 1.3$. Furthermore, magnetic shear is also an important parameter,

and high values of shear—in conjunction with low values of q—contribute to the absence of electromagnetic effects and modes.

Nonlinear simulations performed for the TEM-unstable discharge showed strong zonal flows and a significant Dimits-like shift, with the nonlinear threshold density gradient approximately three times the value of the linear critical gradient. Although the experiment seems to be operating near marginal stability, the simulations yield transport levels well below that of experimental measurements on MST. To investigate the effect of residual tearing mode fluctuations, a small, resonant radial magnetic field perturbation was imposed, which served to greatly reduce the zonal flow strength and bring transport fluxes up to levels more in line with experiment. In general, this work reveals that microinstability-driven transport may be sufficient to explain experimental transport levels, but work remains to be done to better determine important experimental quantities such as gradients and magnetic diffusivity/residual tearing mode stochasticity. This presents important topics for future work and an area for fruitful collaboration between theory and experiment.

[1]B. E. Chapman, A. F. Almagri, J. K. Anderson, T. M. Biewer, P. K. Chattopadhyay, C.-S. Chiang, D. Craig, D. J. Den Hartog, G. Fiksel, C. B. Forest, A. K. Hansen, D. Holly, N. E. Lanier, R. O'Connell, S. C. Prager, J. C. Reardon, J. S. Sarff, M. D. Wyman, D. L. Brower, W. X. Ding, Y. Jiang, S. D. Terry, P. Franz, L. Marrelli, and P. Martin, Phys. Plasmas **9**, 2061 (2002).
[2]D. Carmody, M. J. Pueschel, and P. W. Terry, Phys. Plasmas **20**, 052110 (2013).
[3]I. Predebon and F. Sattin, Phys. Plasmas **20**, 040701 (2013).
[4]I. Predebon, F. Sattin, M. Veranda, D. Bonfiglio, and S. Cappello, Phys. Rev. Lett. **105**, 195001 (2010).
[5]I. Predebon, C. Angioni, and S. C. Guo, Phys. Plasmas **17**, 012304 (2010).
[6]V. Tangri, P. W. Terry, and R. E. Waltz, Phys. Plasmas **18**, 052310 (2011).
[7]R. N. Dexter, D. W. Kerst, T. W. Lovell, S. C. Prager, and J. C. Sprott, Fusion Technol. **19**, 131 (1991).
[8]A. M. Dimits, G. Bateman, M. A. Beer, B. I. Cohen, W. Dorland, G. W. Hammett, C. Kim, J. E. Kinsey, M. Kotschenreuther, A. H. Kritz, L. L. Lao, J. Mandrekas, W. M. Nevins, S. E. Parker, A. J. Redd, D. E. Shumaker, R. Sydora, and J. Weiland, Phys. Plasmas **7**, 969 (2000).
[9]D. R. Ernst, P. T. Bonoli, P. J. Catto, W. Dorland, C. L. Fiore, R. S. Granetz, M. Greenwald, A. E. Hubbard, M. Porkolab, M. H. Redi, J. E. Rice, and K. Zhurovich, Phys. Plasmas **11**, 2637 (2004).
[10]D. R. Ernst, N. Basse, W. Dorland, C. L. Fiore, L. Lin, A. Long, M. Porkolab, K. Zeller, and K. Zhurovich, paper IAEA-CN-149/TH/1-3, Proceedings of 21st International Atomic Energy Agency Fusion Energy Conference, Chengdu, China, 2006.

[11]D. R. Ernst, "Nonlinear upshift of trapped electron mode critical density gradient: Simulation and experiment," APS Meeting Abstracts, 2012, Vol. 1.

[12]J. Lang, Y. Chen, and S. E. Parker, Phys. Plasmas **14**, 082315 (2007).

[13]J. Lang, S. E. Parker, and Y. Chen, Phys. Plasmas **15**, 055907 (2008).

[14]F. Jenko, W. Dorland, M. Kotschenreuther, and B. N. Rogers, Phys. Plasmas **7**, 1904 (2000).

[15]See http://gene.rzg.mpg.de for code details and access.

[16]X. Lapillonne, S. Brunner, T. Dannert, S. Jolliet, A. Marinoni, L. Villard, T. Görler, F. Jenko, and F. Merz, Phys. Plasmas **16**, 032308 (2009).

[17]B. E. Chapman, J. W. Ahn, A. F. Almagri, J. K. Anderson, F. Bonomo, D. L. Brower, D. R. Burke, K. Caspary, D. J. Clayton, S. K. Combs, W. A. Cox, D. Craig, B. H. Deng, D. J. Den Hartog, W. X. Ding, F. Ebrahimi, D. A. Ennis, G. Fiksel, C. B. Forest, C. R. Foust, P. Franz, S. Gangadhara, J. A. Goetz, M. C. Kaufman, J. G. Kulpin, A. Kuritsyn, R. M. Magee, M. C. Miller, V. V. Mirnov, P. D. Nonn, R. O'Connell, S. P. Oliva, S. C. Prager, J. A. Reusch, J. S. Sarff, H. D. Stephens, M. D. Wyman, and T. Yates, Nucl. Fusion **49**, 104020 (2009).

[18]J. K. Anderson, C. B. Forest, T. M. Biewer, J. S. Sarff, and J. C. Wright, Nucl. Fusion **44**, 162–171 (2004).

[19]G. Rewoldt and W. M. Tang, Phys. Fluids B: Plasma Phys. **2**, 318 (1990).

[20]D. R. Ernst, J. Lang, W. M. Nevins, M. Hoffman, Y. Chen, W. Dorland, and S. Parker, Phys. Plasmas **16**, 055906 (2009).

[21]M. Kammerer, F. Merz, and F. Jenko, Phys. Plasmas **15**, 052102 (2008).

[22]A. Hirose, Phys. Plasmas **7**, 433 (2000).

[23]M. J. Pueschel, M. Kammerer, and F. Jenko, Phys. Plasmas **15**, 102310 (2008).

[24]M. J. Pueschel and F. Jenko, Phys. Plasmas **17**, 062307 (2010).

[25]J. Citrin, F. Jenko, P. Mantica, D. Told, C. Bourdelle, R. Dumont, J. Garcia, J. W. Haverkort, G. M. D. Hogeweij, T. Johnson, M. J. Pueschel, and JET-EFDA contributors, Nucl. Fusion **54**, 023008 (2014).

[26]B. Coppi, S. Migliuolo, and Y.-K. Pu, Phys. Fluids B: Plasma Phys. **2**, 2322 (1990).

[27]J. Candy and R. E. Waltz, J. Comput. Phys. **186**, 545 (2003).

[28]A. Ishizawa, T.-H. Watanabe, H. Sugama, S. Maeyama, and N. Nakajima, Phys. Plasmas **21**, 055905 (2014).

[29]C. Z. Cheng, Phys. Fluids **25**, 1020 (1982).

[30]R. Y. Dagazian and R. B. Paris, Plasma Phys. **24**, 661 (1982).

[31]J. Wesson, *Tokamaks* (Oxford University Press, London, 1997).

[32]P. H. Diamond, S.-I. Itoh, K. Itoh, and T. S. Hahm, Plasma Phys. Controlled Fusion **47**, R35 (2005).

[33]D. R. Hatch, P. W. Terry, W. M. Nevins, and W. Dorland, Phys. Plasmas **16**, 022311 (2009).

[34]T. Görler, Ph.D. thesis, University of Ulm, 2009.

[35]P. W. Terry, Rev. Mod. Phys. **72**, 109 (2000).

[36]K. D. Makwana, P. W. Terry, J.-H. Kim, and D. R. Hatch, Phys. Plasmas **18**, 012302 (2011).

[37]K. D. Makwana, P. W. Terry, and J.-H. Kim, Phys. Plasmas **19**, 062310 (2012).

[38]K. D. Makwana, P. W. Terry, M. J. Pueschel, and D. R. Hatch, Phys. Rev. Lett. **112**, 095002 (2014).

[39]R. E. Waltz, G. M. Staebler, W. Dorland, G. W. Hammett, M. Kotschenreuther, and J. A. Konings, Phys. Plasmas **4**, 2482 (1997).

[40]M. A. Beer, Ph. D. thesis, Princeton University, 1994.

[41]T. S. Hahm, M. A. Beer, Z. Lin, G. W. Hammett, W. W. Lee, and W. M. Tang, Phys. Plasmas **6**, 922 (1999).

[42]P. Xanthopoulos, F. Merz, T. Görler, and F. Jenko, Phys. Rev. Lett. **99**, 035002 (2007).

[43]J. S. Sarff, A. F. Almagri, J. K. Anderson, T. M. Biewer, A. P. Blair, M. Cengher, B. E. Chapman, P. K. Chattopadhyay, D. Craig, D. J. Den Hartog, F. Ebrahimi, G. Fiksel, C. B. Forest, J. A. Goetz, D. Holly, B. Hudson, T. W. Lovell, K. J. McCollam, P. D. Nonn, R. O'Connell, S. P. Oliva, S. C. Prager, J. C. Reardon, M. A. Thomas, M. D. Wyman, D. L. Brower, W. X. Ding, S. D. Terry, M. D. Carter, V. I. Davydenko, A. A. Ivanov, R. W. Harvey, R. I. Pinsker, and C. Xiao, Nucl. Fusion **43**, 1684 (2003).

[44]W. M. Nevins, E. Wang, and J. Candy, Phys. Rev. Lett. **106**, 065003 (2011).

[45]E. Wang, W. M. Nevins, J. Candy, D. Hatch, P. Terry, and W. Guttenfelder, Phys. Plasmas **18**, 056111 (2011).

[46]D. R. Hatch, M. J. Pueschel, F. Jenko, W. M. Nevins, P. W. Terry, and H. Doerk, Phys. Rev. Lett. **108**, 235002 (2012).

[47]D. R. Hatch, M. J. Pueschel, F. Jenko, W. M. Nevins, P. W. Terry, and H. Doerk, Phys. Plasmas **20**, 012307 (2013).

[48]P. W. Terry, M. J. Pueschel, D. Carmody, and W. M. Nevins, Phys. Plasmas **20**, 112502 (2013).

[49]M. J. Pueschel, P. W. Terry, F. Jenko, D. R. Hatch, W. M. Nevins, T. Görler, and D. Told, Phys. Rev. Lett. **110**, 155005 (2013).

[50]M. J. Pueschel, D. R. Hatch, T. Görler, W. M. Nevins, F. Jenko, P. W. Terry, and D. Told, Phys. Plasmas **20**, 102301 (2013).

[51]M. J. Pueschel, F. Jenko, M. Schneller, T. Hauff, S. Günter, and G. Tardini, Nucl. Fusion **52**, 103018 (2012).

[52]M. J. Pueschel, P. W. Terry, and D. R. Hatch, Phys. Plasmas **21**, 055901 (2014).

[53]T. Biewer, C. Forest, J. K. Anderson, G. Fiksel, B. Hudson, S. Prager, J. Sarff, J. Wright, D. L. Brower, W. Ding, and S. Terry, Phys. Rev. Lett. **91**, 045004 (2003).

[54]J. B. Taylor, Rev. Mod. Phys. **58**, 741 (1986).

[55]B. Hudson, Ph.D. thesis, University of Wisconsin-Madison, 2006.

[56]A. B. Rechester and M. Rosenbluth, Phys. Rev. Lett. **40**, 38 (1978).

[57]M. J. Pueschel, T. Görler, F. Jenko, D. R. Hatch, and A. J. Cianciara, Phys. Plasmas **20**, 102308 (2013).